Editors' Suggestion

Topological Amorphous Metals

Yan-Bin Yang,[1] Tao Qin,[2] Dong-Ling Deng,[1] L.-M. Duan,[1] and Yong Xu[1*]
[1]Center for Quantum Information, IIIS, Tsinghua University, Beijing 100084, People's Republic of China
[2]Department of Physics, School of Physics and Materials Science, Anhui University, Hefei, Anhui Province 230601, People's Republic of China

(Received 25 October 2018; revised manuscript received 10 June 2019; published 12 August 2019)

We study amorphous systems with completely random sites and find that, through constructing and exploring a concrete model Hamiltonian, such a system can host an exotic phase of topological amorphous metal in three dimensions. In contrast to the traditional Weyl semimetals, topological amorphous metals break translational symmetry, and thus they cannot be characterized by the first Chern number defined based on the momentum space band structures. Instead, their topological properties will manifest in the Bott index and the Hall conductivity as well as the surface states. By studying the energy band and quantum transport properties, we find that topological amorphous metals exhibit a diffusive metal behavior. We further introduce a practical experimental proposal with electric circuits where the predicted phenomena can be observed using state-of-the-art technologies. Our results open the door to exploring topological gapless phenomena in amorphous systems.

DOI: 10.1103/PhysRevLett.123.076401

Weyl semimetals, three-dimensional (3D) materials with Weyl points in band structures [1–4], have attracted considerable interest [5–23] in recent years owing to their fundamental importance in mimicking Weyl fermions in particle physics and their exotic topological properties. In the context of solid-state materials, the linear energy band dispersion around a Weyl point determines the semimetal property with a zero density of states (DOS) at zero energy. In addition, the Weyl point is protected by the first Chern number defined by the integral of Berry curvatures over a closed surface in momentum space enclosing the point [24], leading to a Fermi arc consisting of surface states. This topological feature gives rise to the topological anomalous Hall effect [6,7]. Beyond Weyl fermions that exist in particle physics, new fermions, such as type II Weyl fermions [25–27] (also called structured Weyl fermions [28]) and high spin fermions [29,30], can appear in topological gapless materials.

All of these topological gapless materials feature the existence of gapless structures in momentum space so that the topological invariants can be further defined there. Yet, this can only be guaranteed in a crystalline material with translational symmetry. Here, we ask whether a topological semimetal or metal can exist in an amorphous system with completely random sites, such as glass materials, where the desired translational symmetry is absent. Recent development of technologies in engineering in quantum systems such as arbitrary positioning of atoms [31,32] and, in mechanical systems, such as constructing interacting gyroscopes [33] have paved the way for fabricating amorphous materials. However, the study of topological phenomena in amorphous systems is still in its infancy stage, and only a few works demonstrating the existence of topological insulators in amorphous systems have been published [33–40]. Whether topological semimetals or metals exist in amorphous systems has not been explored hitherto.

In this paper, we demonstrate, by constructing and exploring a model Hamiltonian, the existence of a topological metal phase in a 3D amorphous system. The system is generated by randomly sampling sites in a box (see Fig. 1 for one sample configuration), and the results are obtained by averaging over many sample configurations. We find three distinct phases—namely, the topological amorphous metal (TAM), amorphous Anderson insulator (AAI), and amorphous insulator (AI) phases. In contrast to Weyl semimetals with translational symmetry, where their topology can be characterized by the first Chern number, the

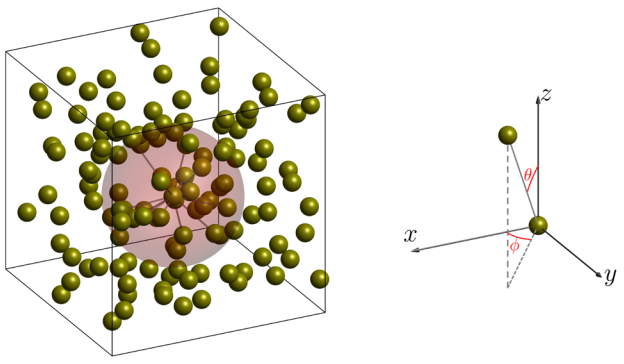

FIG. 1. Schematic of a 3D random site configuration with the allowed hopping inside the light red sphere for a typical site at the center.

topological feature of our amorphous system is identified using the Bott index, the Hall conductivity, and the surface states. To determine whether a phase in the amorphous system is a metal, a semimetal, or an insulator, we compute the band properties including the energy gap, the DOS, the level statistics, and the inverse participation ratio, and the transport properties including the longitudinal conductivity and the Fano factor. We find that, in the majority of the parameter region where the Bott index and the Hall conductivity are nonzero, the system is gapless, exhibiting a diffusive metal behavior. The other regions correspond to the insulating phase where the longitudinal conductivity drops to zero and the Fano factor suddenly rises to 1. The insulator can be further divided into the AAI with a nonzero DOS and the AI with a zero DOS. Finally, we introduce a practical scheme to realize such a Hamiltonian and observe its related exotic phenomena in electric circuits.

Model Hamiltonian.—We start by constructing the following model Hamiltonian,

$$H = \sum_{\mathbf{x}} \left[\sum_{\mathbf{R}} t(R) \hat{c}^{\dagger}_{\mathbf{x}} H_0(\theta, \phi) \hat{c}_{\mathbf{x}+\mathbf{R}(\theta,\phi)} + m_z \hat{c}^{\dagger}_{\mathbf{x}} \sigma_z \hat{c}_{\mathbf{x}} \right], \quad (1)$$

where $\hat{c}^{\dagger}_{\mathbf{x}} = (\hat{c}^{\dagger}_{\mathbf{x},\uparrow}, \hat{c}^{\dagger}_{\mathbf{x},\downarrow})$, with $\hat{c}^{\dagger}_{\mathbf{x},\sigma}$ creating a fermion with spin σ at the position $\mathbf{x}$, which is a random vector uniformly distributed in the box, $x_\nu \in (0, L_\nu)$ with $\nu = x, y, z$, $\mathbf{R}(\theta, \phi)$ denotes the neighboring sites shown in Fig. 1, σ_ν ($\nu = x, y, z$) are the Pauli matrices, and m_z is the mass term. $H_0(\theta, \phi) = \sigma_z + i \sin\theta \cos\phi \sigma_x + i \sin\theta \sin\phi \sigma_y$ describes the hopping matrix for the neighboring sites shown in Fig. 1. We are inspired to construct such a Hamiltonian by the fact that it reduces to a well-studied Weyl semimetal model [3] when only the nearest-neighbor hopping is considered. In light of irregular sites, we consider a case where the hopping strength decays exponentially, $t(R) = -e^{\lambda(1-R)}/2$, with R being the spatial distance between two sites, where we have chosen the units of energy and length to be 1 for simplicity. Here, we take $\lambda = 3$, the cutoff distance $R_c = 2.5$ so that the hopping is neglected when $R > R_c$ [41], and the site density $\rho = N/V = 1$, where N is the number of sites and $V = L_x L_y L_z$ is the volume of the system. For randomly distributed sets of $\mathbf{x}$, the system does not respect translational, time-reversal, or inversion symmetries. Owing to the random character, for numerical calculation, all of our results are averaged over 180–600 sample configurations.

In Fig. 2(a), we map out the phase diagram with respect to the mass m_z incorporating three distinct phases (assuming that the Fermi surface lies at zero energy): the TAM, AAI, and AI phases, according to the Bott index (or Hall conductivity) and the band and transport properties, which will be discussed in detail in the following. For a topological phase, the Bott index $\mathcal{B}$ is nonzero. For a diffusive metal, the energy gap is zero, the DOS and conductivity are nonzero, and the Fano factor is $1/3$. For an insulator, the conductivity is zero and the Fano factor is 1. In our system, there are two types of insulators: the Anderson insulator with a nonzero DOS and the band insulator with a zero DOS. Our results are summarized in Table I.

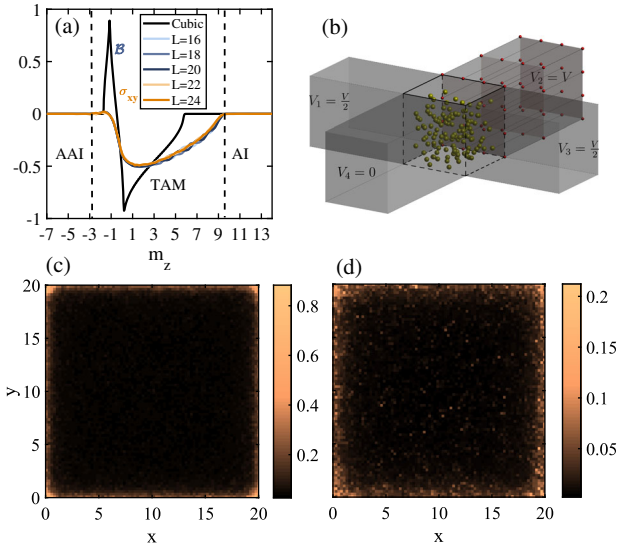

FIG. 2. (a) The Bott index and the Hall conductivity in units of $e^2/(2h)$ as a function of m_z for distinct system sizes. The black line denotes the Bott index for a cubic lattice configuration. Three different phases are identified: amorphous Anderson insulator (AAI), topological amorphous metal (TAM), and amorphous insulator (AI). (b) Schematic of a four terminal setup used to compute the Hall conductivity, where we consider the cubic geometry for all leads (see the dotted part for $V_2 = V$). (c), (d) The local density of states for $m_z = 2$ and $m_z = 6$, respectively.

Bott index and Hall conductivity.—In order to characterize the topology of the 3D amorphous system, we generalize the Bott index $\mathcal{B}$ originally defined in 2D [45] by defining it as

$$\mathcal{B} = \frac{1}{2\pi L_z} \mathrm{Im}\mathrm{Tr} \log(\tilde{U}_y \tilde{U}_x \tilde{U}_y^{\dagger} \tilde{U}_x^{\dagger}), \quad (2)$$

where $\tilde{U}_x$ and $\tilde{U}_y$ are the reduced matrices for $U_x = \hat{P} e^{2\pi i \hat{x}/L_x} \hat{P}$ and $U_y = \hat{P} e^{2\pi i \hat{y}/L_y} \hat{P}$ in the occupied space, respectively. Here, $\hat{x}$ and $\hat{y}$ are the position operators, and $\hat{P}$ is the projection operator for the occupied space. As we are interested in the case in which the Fermi energy lies at zero energy, we consider the states with negative energy as the occupied space for calculating the Bott index. We prove that this generalized Bott index is equivalent to the

TABLE I. Topological, band, and transport properties of three distinct phases. Note that, in the AI phase, the states around the zero energy are localized with LSR ~ 0.39 and IPR > 0.

Phase	$\lvert\mathcal{B}\rvert$ ($\lvert\sigma_{xy}\rvert$)	$\rho(0)$	Gap	$\lvert\sigma_{zz}\rvert$	Fano factor	LSR	IPR
TAM	> 0	> 0	~ 0	> 0	$\sim 1/3$	~ 0.6	~ 0
AAI	~ 0	> 0	~ 0	~ 0	~ 1	~ 0.39	> 0
AI	~ 0	~ 0	> 0	~ 0	~ 1	$\cdots$	$\cdots$

topological anomalous Hall conductivity for a Weyl semimetal (which need not be quantized) in Ref. [41].

In Fig. 2(a), we plot the Bott index as a function of m_z for different system sizes. Remarkably, the amorphous system exhibits nonzero values for the Bott index when $-2.8 \lesssim m_z \lesssim 9.6$, suggesting the topological feature of the system. Compared to the cubic lattice configuration, there appears a topologically nontrivial region for the amorphous system, which is topologically trivial in a crystalline one. We can also observe that the absolute value of the Bott index is no longer symmetric with respect to m_z [46] when the long-range hopping is involved; this explains why there only exists a very small region with the positive Bott index. In addition, the Bott index in the TAM region exhibits several plateaus whose locations change with respect to the system size, reflecting the finite size effect, similar to the case of a crystalline Weyl semimetal.

To show that the Bott index reflects the Hall conductivity in a randomized system, we numerically calculate the Hall conductivity using the Landauer-Büttiker formula in a mesoscopic system. We consider four ideal leads connected to the amorphous system in the x and y directions as schematically shown in Fig. 2(b), as we expect a surface state to appear on the surfaces vertical to these directions. Under the voltage $V_1 = V_3 = V/2$, $V_2 = V$, and $V_4 = 0$, the Hall conductivity is given by [47]

$$\sigma_{xy} = \frac{e^2}{2hL_z}(T_{32} - T_{34}), \tag{3}$$

where T_{mn} is the total transmission probability from lead n to m, which is computed using the nonequilibrium Green's function method [47,48]. As $T_{32} - T_{34}$ accounts for the contribution from chiral edge modes, for a Weyl semimetal, σ_{xy} is equivalent to the Bott index multiplied by $e^2/(2h)$, and we expect this equivalence also to hold in an amorphous system.

In Fig. 2(a), we show the Hall conductivity in comparison to the Bott index. We notice the clear consistence between them in a wide range of m_z in an amorphous system, as we expected. For the slight discrepancy, we estimate that it is caused by finite size effects of the Bott index, which exhibits conspicuous variations for distinct system sizes; the Hall conductivity does not show clear finite size effects when $L = 24$, as their difference from $L = 22$ is small (we consider a cubic case, $L_x = L_y = L_z = L$). Further, the Hall conductivity does not exhibit clear plateaus from finite size effects, probably due to the smearing out around the gap closing region, as in Weyl semimetals. The nonzero Hall conductivity and Bott index suggest the existence of a topological amorphous phase in a wide range of parameters.

To further identify the topological feature of the system, we calculate the local DOS defined as $\rho(E, \mathbf{x}) = [\sum_i \delta(E - E_i)(|\Psi_{E_i,\uparrow\mathbf{x}}|^2 + |\Psi_{E_i,\downarrow\mathbf{x}}|^2)]$, where E_i is the ith eigenvalue, $\Psi_{E_i,\sigma\mathbf{x}}$ with $\sigma = \uparrow, \downarrow$ are the corresponding components of the eigenstate of the system, and $[\cdots]$ denotes the average over samples. The DOS is defined as $\rho(E) = \sum_{\mathbf{x}} \rho(E, \mathbf{x})/(2N)$, which is normalized to 1, i.e., $\int dE \rho(E) = 1$. In Figs. 2(c) and 2(d), we illustrate the local DOS summed over x_z: $\sum_{x_z} \rho(E = 0, \mathbf{x})$ for a system $L_x = L_y = 20$ and $L_z = 10$ for two typical values of m_z, clearly showing the presence of the surface states localized on the boundaries [41].

Band properties.—To discriminate the metal or semimetal phase from the insulator phase with respect to m_z, we compute the gap, twice the lowest positive energy, using the Lanczos algorithm, and the DOS for large systems using the kernel polynomial method (KPM), which expands the DOS in Chebyshev polynomials to the order N_c [49].

Figures 3(a) and 3(b) illustrate the gap and the DOS at zero energy $\rho(E = 0)$ with respect to the mass m_z for distinct system sizes. Clearly, we see that the region with nonzero Bott index from $-2.8 \lesssim m_z \lesssim 9$ corresponds to the gapless region: The gap for $-3.2 < m_z < 2$ is very small even for a small system size (see the red line for $L = 16$) associated with a relative large DOS. $\rho(E = 0)$ reaches the maximum at $m_z = -1.6$, where $\rho(E)$ versus E exhibits a steep peak at zero energy, as shown in Fig. 3(c), and it decreases sharply as m_z moves away from this point

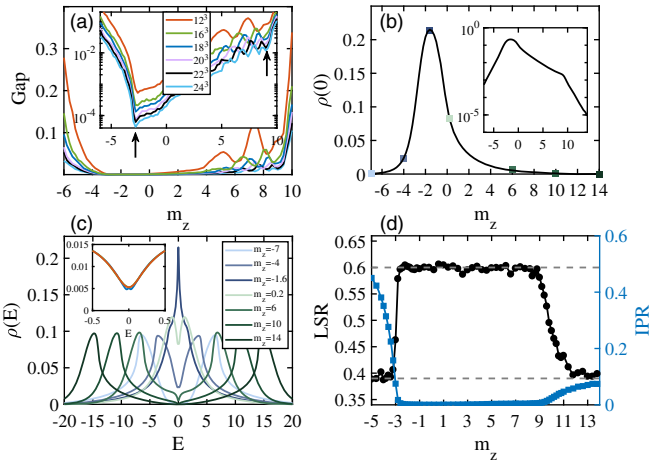

FIG. 3. (a) The gap versus m_z for different system sizes calculated via the Lanczos method, with the inset plotting the same thing in the logarithmic scale. The arrows show the universal dips. (b) The DOS at zero energy $\rho(0)$ as a function of m_z (with the logarithmic scale figure shown in the inset) calculated by the KPM for $L = 55$ and $N_c = 2^{11}$. (c) The DOS $\rho(E)$ versus E for various m_z in different phases for $L = 55$ and $N_c = 2^{11}$. (Inset) Plots of $\rho(E)$ versus E when $m_z = 6$ for $L = 55$, $N_c = 2^{11}$ (red line), $L = 60$, $N_c = 2^{11}$ (green line), and $L = 60$, $N_c = 2^{13}$ (blue line). (d) The level-spacing ratio (LSR) $r(E = 0)$ (left vertical axis) and inverse participation ratio (IPR) $I(E = 0)$ (right vertical axis) for $L = 24$ for the states around zero energy (only the states with negative energy are considered) computed via the Lanczos algorithm. In all the above subfigures, samples in a cubic box are considered.

associated with a developed minimum around zero energy for $\rho(E)$ [see Fig. 3(c)]. When $2 \lesssim m_z \lesssim 9$, while the energy gap strongly depends on the system size, its overall decline with an increasing system size can be observed, suggesting that this phase may be a semimetal or metal. Figure 3(b) further shows that $\rho(E=0)$ does not vanish in this region despite being small, implying that they correspond to a metal phase instead of a semimetal one. Specifically, for $m_z = 6$, $\rho(E)$ shows a sudden drop around zero energy [see Fig. 3(c)], but this minimum does not vanish. To exclude the finite size effect, we calculate $\rho(E)$ using a larger system size and N_c and do not find conspicuous decline of $\rho(E=0)$, as shown in the inset of Fig. 3(c) [41], in stark contrast to a dramatic drop in a Weyl semimetal with quasiperiodic disorder [22].

Viewing Fig. 3(a) in the logarithmic system (see the inset), we clearly see that there appears a universal dip of the energy gap for different system sizes at $m_z = 9$ and $m_z = -2.8$. For the former, $\rho(E=0)$ exhibits a rapid decline to zero as m_z increases from this point [see the inset in Fig. 3(b)], suggesting a phase transition to a band insulator [see $\rho(E)$ versus E for $m_z = 10$, 14 in Fig. 3(c)]. More interestingly, for the latter, the DOS does not vanish and does not show clear nonanalytic behavior with respect to m_z. This phase is actually the Anderson localized insulator (dubbed the amorphous Anderson insulator), which will be identified by the level-spacing statistics, the inverse participation ratio (IPR), the conductivity, and the Fano factor. We note that, with the further decline of m_z, the system develops into a band insulator [see $\rho(E)$ versus E for $m_z = -7$ in Fig. 3(c)], but we cannot identify the transition point since the DOS becomes very small.

For level statistics, we calculate the adjacent level-spacing ratio (LSR): $r(E) = [(1/(N_E - 2))\sum_i \min(\delta_i, \delta_{i+1})/\max(\delta_i, \delta_{i+1})]$, where $\delta_i = E_i - E_{i-1}$, with E_i being the ith eigenenergy sorted in an ascending order, and where $\sum_i$ is the sum over an energy bin around the energy E, with N_E being the energy levels counted. It is well known that for localized states, $r \approx 0.39$ [50] associated with the Poisson statistics and for extended states, $r \approx 0.6$ corresponding to the Gaussian unitary ensemble [51]. Another signature we use is the real space IPR: $I(E) = [(1/N_E)\sum_i \sum_{\mathbf{x}} (|\Psi_{E_i,\uparrow\mathbf{x}}|^2 + |\Psi_{E_i,\downarrow\mathbf{x}}|^2)^2]$, which measures how much a state around energy E is spatially localized. For a completely extended state in an infinitely large system, it is zero; for a state localized in a single site, it is 1.

Figure 3(d) shows that, in the topological metal regime, $r(E=0)$ is around 0.6 and $I(E=0)$ is almost zero; when m_z decreases from -2.8, $r(E=0)$ drops to around 0.39 and $I(E=0)$ increases sharply, indicating the phase transition from the extended phase to the localized one. Interestingly, we also see a similar change of the LSR and the IPR around $m_z \sim 9$, implying that the states around zero energy are localized even though the DOS becomes very small [41].

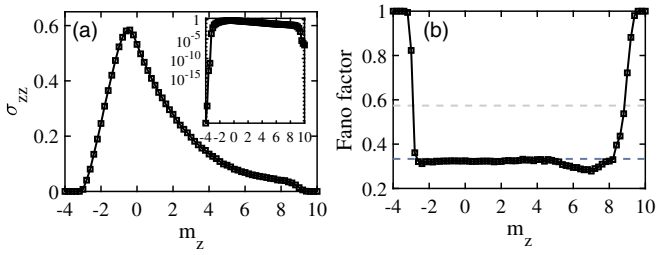

FIG. 4. (a) Conductivity σ_{zz} in units of e^2/h and (b) Fano factor versus m_z for $L = 25$ in a cubic box. (Inset) Plots of the conductivity in the logarithmic scale, showing its steep drops across the phase transitions. The dashed lines correspond to $F = 1/3$ and $F = 1/3 + 1/(6\ln 2)$, respectively.

Conductivity and Fano factor.—To study the quantum transport properties of the amorphous system, we numerically calculate the transmission matrix $tt^\dagger$ at zero energy by the nonequilibrium Green's function method [47,48] and determine the zero-temperature conductance by the Landauer formula $G = (e^2/h)\mathrm{Tr}(tt^\dagger)$ [47] and the Fano factor $F = \mathrm{Tr}[tt^\dagger(1 - tt^\dagger)]/\mathrm{Tr}(tt^\dagger)$ [9,52] for a system connected to two ideal terminals for $z < 0$ and $z > L_z$.

Figure 4(a) shows the conductivity $\sigma_{zz} = LG/W^2$ versus m_z, with W and L being the width and length of the system (we here consider a cubic box geometry, i.e., $W = L$). The conductivity is nonzero in the region with nonzero Bott index from $-2.8 \lesssim m_z \lesssim 9$, showing a diffusive metal behavior; as for a pseudoballistic semimetal, the conductivity vanishes [9]. The conductivity drops to zero at around $m_z \sim -2.8$ and at around $m_z \sim 9$ when m_z moves away to the left and right regions, respectively. The former corresponds to the transition into the Anderson insulator phase, the latter the band insulator phase with vanishing DOS. The diffusive metal behavior is also reflected in the Fano factor that takes the value around $F = 1/3$ [52] [see Fig. 4(b)]. The transition into the insulator phase is signaled by the steep rise of the Fano factor to 1 due to the Poisson process. We do not find any discernible region where the Fano factor takes the value of $F_0 = 1/3 + 1/(6\ln 2)$ for Weyl semimetals without disorder [9], further suggesting the absence of the semimetal phase [41].

Experimental realization.—Topological amorphous metals may be realized in classical systems, artificial quantum systems, and solid-state glass materials. Here, we propose an experimental scheme to engineer a Laplacian (acting as a Hamiltonian) with electric circuits, which takes the form of our Hamiltonian [41]. The surface states can be observed by measuring the two-point impedance. Recently, a number of topological phases, such as the Su-Schrieffer-Heeger model [53], Weyl semimetals [54], and higher topological insulators [55] have been experimentally observed with electric circuits. In addition, recent development of technology has allowed us to place Rydberg atoms in arbitrary geometry using optical tweezers [31,32], which makes it possible to realize our model in this system.

In summary, we discover a topological amorphous metal phase in 3D amorphous systems. We identify its topological feature by calculating the Bott index, the Hall conductivity, and the surface states. Through further study of its band properties including the energy gap, DOS, LSR, and IPR and the quantum transport properties, we find that the topological phase exhibits a diffusive metal behavior. We further predict the phase transition from the topological metal phase to the Anderson insulator phase and the band insulator phase with respect to a system parameter. Our results open a new avenue for studying topological gapless phenomena in amorphous systems. These new phenomena might be observed in various amorphous materials, such as engineered classical or atomic systems and glass materials.

We thank A. Agarwala, H. Jiang, S.-G. Cheng, and H.-W. Liu for the helpful discussions. Y.-B. Y. and Y. X. are supported by the start-up fund from Tsinghua University (Grant No. 53330300219) and the National Thousand-Young-Talents Program (Grant No. 042003003). T. Q. is supported by the start-up fund (Grant No. S020118002/069) from Anhui University. D.-L. D. acknowledges the start-up fund from Tsinghua University. L.-M. D. is supported by the Ministry of Education and the National Key Research and Development Program of China (Grant No. 2016YFA0301902).

*yongxuphy@tsinghua.edu.cn

[1] A. A. Burkov, Nat. Mater. **15**, 1145 (2016).
[2] S. Jia, S.-Y. Xu, and M. Z. Hasan, Nat. Mater. **15**, 1140 (2016).
[3] N. P. Armitage, E. J. Mele, and A. Vishwanath, Rev. Mod. Phys. **90**, 015001 (2018).
[4] Y. Xu, Front. Phys. **14**, 43402 (2019).
[5] X. Wan, A. M. Turner, A. Vishwanath, and S. Y. Savrasov, Phys. Rev. B **83**, 205101 (2011).
[6] K.-Y. Yang, Y.-M. Lu, and Y. Ran, Phys. Rev. B **84**, 075129 (2011).
[7] A. A. Burkov and L. Balents, Phys. Rev. Lett. **107**, 127205 (2011).
[8] G. Xu, H. Weng, Z. Wang, X. Dai, and Z. Fang, Phys. Rev. Lett. **107**, 186806 (2011).
[9] B. Sbierski, G. Pohl, E. J. Bergholtz, and P. W. Brouwer, Phys. Rev. Lett. **113**, 026602 (2014).
[10] T. Dubček, C. J. Kennedy, L. Lu, W. Ketterle, M. Soljačić, and H. Buljan, Phys. Rev. Lett. **114**, 225301 (2015).
[11] E. J. Bergholtz, Z. Liu, M. Trescher, R. Moessner, and M. Udagawa, Phys. Rev. Lett. **114**, 016806 (2015).
[12] H. Weng, C. Fang, Z. Fang, B. A. Bernevig, and X. Dai, Phys. Rev. X **5**, 011029 (2015).
[13] S. A. Yang, H. Pan, and F. Zhang, Phys. Rev. Lett. **115**, 156603 (2015).
[14] C.-Z. Chen, J. Song, H. Jiang, Q.-F. Sun, Z. Wang, and X. C. Xie, Phys. Rev. Lett. **115**, 246603 (2015).
[15] S.-Y. Xu *et al.*, Science **349**, 613 (2015).
[16] B. Q. Lv, H. M. Weng, B. B. Fu, X. P. Wang, H. Miao, J. Ma, P. Richard, X. C. Huang, L. X. Zhao, G. F. Chen, Z. Fang, X. Dai, T. Qian, and H. Ding, Phys. Rev. X **5**, 031013 (2015).
[17] L. Lu, Z. Wang, D. Ye, L. Ran, L. Fu, J. D. Joannopoulos, and M. Soljačić, Science **349**, 622 (2015).
[18] Y. Zhang, D. Bulmash, P. Hosur, A. C. Potter, and A. Vishwanath, Sci. Rep. **6**, 23741 (2016).
[19] J. H. Pixley, D. A. Huse, and S. Das Sarma, Phys. Rev. X **6**, 021042 (2016).
[20] H. Ishizuka, T. Hayata, M. Ueda, and N. Nagaosa, Phys. Rev. Lett. **117**, 216601 (2016).
[21] Y. Xu and L.-M. Duan, Phys. Rev. A **94**, 053619 (2016).
[22] J. H. Pixley, J. H. Wilson, D. A. Huse, and S. Gopalakrishnan, Phys. Rev. Lett. **120**, 207604 (2018).
[23] S. V. Syzranov and L. Radzihovsky, Annu. Rev. Condens. Matter Phys. **9**, 35 (2018).
[24] G. E. Volovik, *The Universe in a Helium Droplet* (Oxford University Press, Oxford, 2003).
[25] A. A. Soluyanov, D. Gresch, Z. Wang, Q. Wu, M. Troyer, X. Dai, and B. A. Bernevig, Nature (London) **527**, 495 (2015).
[26] K. Deng *et al.*, Nat. Phys. **12**, 1105 (2016).
[27] L. Huang, T. M. McCormick, M. Ochi, Z. Zhao, M.-T. Suzuki, R. Arita, Y. Wu, D. Mou, H. Cao, J. Yan, N. Trivedi, and A. Kaminski, Nat. Mater. **15**, 1155 (2016).
[28] Y. Xu, F. Zhang, and C. Zhang, Phys. Rev. Lett. **115**, 265304 (2015).
[29] B. Bradlyn, J. Cano, Z. Wang, M. G. Vergniory, C. Felser, R. J. Cava, and B. A. Bernevig, Science **353**, aaf5037 (2016).
[30] B. Q. Lv, Z.-L. Feng, Q.-N. Xu, X. Gao, J.-Z. Ma, L.-Y. Kong, P. Richard, Y.-B. Huang, V. N. Strocov, C. Fang, H.-M. Weng, Y.-G. Shi, T. Qian, and H. Ding, Nature (London) **546**, 627 (2017).
[31] D. Barredo, S. de Léséleuc, V. Lienhard, T. Lahaye, and A. Browaeys, Science **354**, 1021 (2016).
[32] M. Endres, H. Bernien, A. Keesling, H. Levine, E. R. Anschuetz, A. Krajenbrink, C. Senko, V. Vuletic, M. Greiner, and M. D. Lukin, Science **354**, 1024 (2016).
[33] N. P. Mitchell, L. M. Nash, D. Hexner, A. M. Turner, and W. T. M. Irvine, Nat. Phys. **14**, 380 (2018).
[34] A. Agarwala and V. B. Shenoy, Phys. Rev. Lett. **118**, 236402 (2017).
[35] S. Mansha and Y. D. Chong, Phys. Rev. B **96**, 121405(R) (2017).
[36] M. Xiao and S. Fan, Phys. Rev. B **96**, 100202(R) (2017).
[37] C. Bourne and E. Prodan, J. Phys. A **51**, 235202 (2018).
[38] K. Pöyhönen, I. Sahlberg, A. Westström, and T. Ojanen, Nat. Commun. **9**, 2103 (2018).
[39] E. L. Minarelli, K. Pöyhönen, G. A. R. van Dalum, T. Ojanen, and L. Fritz, Phys. Rev. B **99**, 165413 (2019).
[40] G.-W. Chern, Europhys. Lett. **126**, 37002 (2019).
[41] See Supplemental Material at http://link.aps.org/supplemental/10.1103/PhysRevLett.123.076401, which includes Refs. [42–44], for more details on the proof of the equivalence between the Bott index and the Hall conductivity, the Griffiths region, the surface states, the discussion on semimetal phases, the mobility edges, the stability against the on-site disorder, and the experimental realization in electric circuits.
[42] Y. Ge and M. Rigol, Phys. Rev. A **96**, 023610 (2017).

[43] T. Hofmann, T. Helbig, C. H. Lee, M. Greiter, and R. Thomale, Phys. Rev. Lett. **122**, 247702 (2019).
[44] W.-K. Chen, *The Circuits and Filters Handbook*, 3rd ed. (CRC Press, Boca Raton, 2009).
[45] T. A. Loring and M. B. Hastings, Europhys. Lett. **92**, 67004 (2010).
[46] Y.-B. Yang, L.-M. Duan, and Y. Xu, Phys. Rev. B **98**, 165128 (2018).
[47] S. Datta, *Electronic Transport in Mesoscopic Systems* (Cambridge University Press, Cambridge, England, 1997).
[48] Y. Xing, Q.-F. Sun, and J. Wang, Phys. Rev. B **75**, 075324 (2007).
[49] A. Weiße, G. Wellein, A. Alvermann, and H. Fehske, Rev. Mod. Phys. **78**, 275 (2006).
[50] V. Oganesyan and D. A. Huse, Phys. Rev. B **75**, 155111 (2007).
[51] L. D'Alessio and M. Rigol, Phys. Rev. X **4**, 041048 (2014).
[52] C. W. J. Beenakker and M. Büttiker, Phys. Rev. B **46**, 1889 (R) (1992).
[53] C. H. Lee, S. Imhof, C. Berger, F. Bayer, J. Brehm, L. W. Molenkamp, T. Kiessling, and R. Thomale, Commun. Phys. **1**, 39 (2018).
[54] Y. Lu, N. Jia, L. Su, C. Owens, G. Juzeli-unas, D. I. Schuster, and J. Simon, Phys. Rev. B **99**, 020302(R) (2019).
[55] S. Imhof, C. Berger, F. Bayer, J. Brehm, L. W. Molenkamp, T. Kiessling, F. Schindler, C. H. Lee, M. Greiter, T. Neupert, and R. Thomale, Nat. Phys. **14**, 925 (2018).